Morphological structure of Gluconacetobacter xylinus cellulose and cellulose-based organic-inorganic composite materials

2017 J. Phys.: Conf. Ser. 848 012017

(http://iopscience.iop.org/1742-6596/848/1/012017)

IOP Conf. Series: Journal of Physics: Conf. Series **848** (2017) 012017 doi:10.1088/1742-6596/848/1/012017

Morphological structure of *Gluconacetobacter xylinus* cellulose and cellulose-based organic-inorganic composite materials

R Yu Smyslov[1, 2, *], K V Ezdakova[2], G P Kopitsa[2, 3], A K Khripunov[1], A N Bugrov[1, 4], A A Tkachenko[5], B Angelov[6], V Pipich[7], N K Szekely[7], A E Baranchikov[8], E Latysheva[9], Yu O Chetverikov[2] and V Haramus[10]

[1] Institute of Macromolecular Compounds RAS, St Petersburg, 199004, Russia
[2] B P Konstantinov Petersburg Nuclear Physics Institute (National Research Center "Kurchatov Institute"), Gatchina, Russia
[3] I V Grebenshchikov Institute of Silicate Chemistry RAS, St Petersburg, Russia
[4] Saint Petersburg Electrotechnical University "LETI", 197376, St Petersburg, Russia
[5] Department of Microbiology, S Petersburg State University, St Petersburg, 199178, Russia
[6] Institute of Physics ASCR, ELI Beamlines, 18000 Prague, Czech Republic
[7] JCNS, Forschungszentrum Juelich GmbH, Outstation at MLZ, 85747, Garching, Germany
[8] N S Kurnakov Institute of General and Inorganic Chemistry RAS, Moscow, Russia
[9] RC of SPbSU "Centre for diagnosis of functional materials in medicine, pharmacology and nanoelectronics", S Petersburg, 198504, Russia
[10] Helmholtz- Zentrum Geesthacht Outstation at EMBL/DESY, Notkestrasse 85, Hamburg, Germany

[*] Author to whom any correspondence should be addressed

E-mail: urs@mail.macro.ru

Abstract. Scanning electron microscopy, ultra-small-angle neutron scattering (USANS), small-angle neutron and X-ray scattering (SANS and SAXS), as well as low-temperature nitrogen adsorption, were used in the studies of micro- and mesostructure of polymer matrix prepared from air-dry preliminarily disintegrated cellulose nano-gel film (synthesized by *Gluconacetobacter xylinus*) and the composites based on this bacterial cellulose. The composites included ZrO_2 nanoparticles, Tb^{3+} in the form of low molecular weight salt and of metal-polymer complex with poly(vinylpyrrolydone)-poly(methacryloyl-*o*-aminobenzoic acid) copolymer. The combined analysis of the data obtained allowed revealing three levels of fractal organization in mesostructure of *G. xylinus* cellulose and its composites. It was shown that both the composition and an aggregation state of dopants have a significant impact on the structural characteristics of the organic-inorganic composites. The composites containing Tb^{3+} ions demonstrate efficient luminescence; its intensity is an order of magnitude higher in the case of the composites with the metal-polymer complex. It was found that there is the optimal content of ZrO_2 nanoparticles in composites resulting in increased Tb^{3+} luminescence.

1. Introduction

In recent years, due to new requirements for quality of materials, great interest has been generated in organic-inorganic composites which are promising materials in various fields including optoelectronics, medicine, cosmetology, textile industry etc. [1–3]. Cellulose-based composites possess natural biodegradability and biocompatibility; they consist of cellulose nanocrystals (**CNs**), which warrants attention because of CNs' unsurpassed physical and chemical properties [4]. Cellulose is one of the most widespread natural polymers on Earth. It is known that cellulose can be obtained from various evolutionary sources; it can be synthesized by plants, some animals (e.g., members of the subphylum *Tunicata*), or bacteria (e.g., *Gluconacetobacter xylinus*). It should be noted that biosynthesis of cellulose performed by various organisms yields products with varying morphological structures which differ significantly in supramolecular organization [5]. At the same time, cellulose biosynthesis by *G. xylinus* is environmentally friendly.

Unlike plants, *G. xylinus* accomplish producing cellulose (**GXC**) on the nano-sized level [6]. GXC synthesized in stationary conditions on the surface of nutrient medium is pellicle, which is able to retain water in the approximate ratio of 1:100 (dry substance : H_2O) [7]. Due to certain physicochemical properties and the unique structure, this nano-gel film (**NGF**) is widely used as a matrix in preparation of various organic-inorganic composite materials (after preliminary treatment). The GXC-based composites containing gold, silver, selenium nanoparticles (**NPs**), TiO_2, SiO_2, CdSe and calcium phosphate NPs have been described [8]. GXC can be used as a scaffold (rigid supramolecular structure) for regeneration of a wide variety of biological tissues. Thus, the authors of [3, 9] demonstrated that GXC can serve as a matrix for mechanical reinforcement of hydrogels from poly(acrylamide), poly(vinyl alcohol) and similar polymers. The presence of hydrophilic synthetic polymers in a material imparts elasticity and the necessary swelling degree, while the rigid-chain base (cellulose) provides strength to a composite. Composite hydrogels reinforced by GXC are similar to different types of cartilage in their water content and mechanical properties; therefore, these materials can be used as substitutes for damaged cartilage fragments [10]. Thus, GXC may become excellent material for medical nanotechnologies [3, 11].

Introducing lanthanides into hybrid polymer matrix allows developing materials with tunable or modulated optical properties [1]. Lanthanide ions possess the unique photophysical properties, which are important for applications in photonics [12–15], for generation and enhancement of laser light [16] or in producing optical amplifiers, *e.g.* erbium-doped fiber amplifiers [17, 18]. Lanthanide ions are widely used in development of light-emitting materials for active light guides in visible and near-infrared spectral regions, active coatings, biomedical devices and chemosensors. Thus, lanthanide ions can be used in numerous areas of material science and technology related to integration, miniaturization and functionality of devices. For example, the membranes based on composites of GXC with ITO and SiO_2 can be used as flexible substrates in producing organic light-emitting diodes [19].

2. Materials and methods

2.1. Biosynthesis of bacterial cellulose by Gluconacetobacter xylinus

Biosynthesis of cellulose was performed by *G. xylinus* (bacterium strain № 1629 CALU deposited at the Department of Microbiology of S. Petersburg State University). The nutrient medium contained aqueous solutions of yeastrel, glucose, peptone, ethanol and beer wort; concentrations of these nutrients were found after optimization of the medium [20, 21]. The pH of the medium was 5.9—6.0. The *G. xylinus* strain cultivated for 48 hrs. in the nutrient medium containing mixture of yeastrel and beer wort (6 degrees Balling) in the 1:1 ratio to the mixture of glucose (2 wt.%) and ethanol (1 vol.%) was used as an inoculum. Biosynthesis of GXC was carried out at 30.0 ± 0.5 °C for 6–7 days; then, cellulose was isolated and washed periodically with renewed boiling aqueous solution of NaOH (concentration 0.5-1%) until all *G. xylinus* cells were removed. Then, in order to remove NaOH, GXC was washed with distilled water, acetic acid (0.5% solution) and again with distilled water until the

neutral pH was achieved. The purified bacterial cellulose (BC) was stored either in the form of NGF in distilled water at 5°C or in autoclave (after sterilization) at room temperature as well as in the dry form (after freeze-drying).

2.2. Synthesis of hybrid organic-inorganic composites

The GXC nano-gel film intended for preparation of composite material was preliminarily disintegrated in laboratory blender at 2000 rpm. Then aqueous suspension of disintegrated NGF was obtained; the necessary amount of ZrO_2 NPs (obtained by hydrothermal method) in the form of powder with an approximate diameter of 200 ± 50 Å [22] was added to cellulose suspension under continuous stirring and ultrasound treatment (35 kHz, 100 W) (*note* K3, K5, K6, K8 on table 1).

Luminescent material was obtained using Tb^{3+}. These ions were introduced into cellulose either in the form of low molecular weight luminophore ($TbCl_3$) or in the form of metal-polymer complex (**MPC**) [Tb(*polyLig*)](III) in aqueous solution. Copolymer of vinyl pyrrolidone (**VP**) with 12 mol.% of methacryloyl-*o*-aminobenzoic acid (**M-*o*-ABA**) or **P(VP-*co*-MABA)** was used as a polymeric ligand (***polyLig***) in the MPC (*note* the copolymer formula in the footnote of table 1) [23].

Sorption of aqueous solution of terbium chloride (III) by suspension of disintegrated GXC was carried out for 24 hrs. In this procedure, we used terbium chloride hexahydrate ($TbCl_3$·6H2O) (99.9% purity) purchased from Sigma-Aldrich (CAS 13798-24-8) without further purification. Aqueous solution of this reactant at a concentration of 0.72 mg/mL was prepared, and the necessary amount of this solution was added to water suspension of GXC (table 1).

Table 1. The composites based on GXC with added Tb^{3+} (in the form of salt or MPC) and ZrO_2 NPs. The values of luminescence efficiency θ are given at an excitation wavelength (λ_{ex}) of 300 nm and at an observation wavelength of 543 nm (equation 4).

System	GXC, *wt.%*	$c_{Tb^{3+}}$, *wt. %*	*Additives*		θ
			MPC*)	ZrO2	
K0	100	0	–	–	0
K1	99.98	0.02	–	–	1
K2	99.8	0.21	–	–	1.40
K3	98.8	0.21	–	1	1.73
K4	97.5	2.50	–	–	0.33
K5	90.7	0.19	–	9.1	0.94
K6	66.6	0.14	–	33.3	1.16
K7	63.6	1.60	34.7	-	7.74
K8	59.8	1.50	32.6	6	11.86

*) the MPC was formed on the base of P(VP-*co*-MABA):

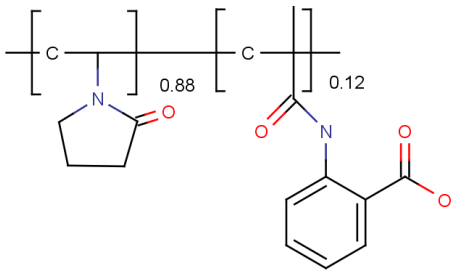

VP M-*o*-ABA

The MPC was prepared beforehand in the following way. Copolymer was dissolved, and side groups of M-*o*-ABA were ionized; then, terbium (III) ions were added in the ratio of [M-*o*-ABA] to

[Tb^{3+}] equal to 4 :1. The obtained complex [Tb(*polyLig*)](III) was added in the necessary amount to aqueous suspension of disintegrated GXC nano-gel film (*note* K7, K8 on table 1).

The prepared aqueous suspensions of disintegrated GXC nano-gel film containing additives were dried in thermostat at 50° C until constant weight was reached, and thus air-dry films of composites were obtained. Composition of materials based on the polymer matrix (air-dry previously disintegrated native GXC) with added ZrO_2 NPs and terbium ions in the form of $TbCl_3$ or [Tb(*polyLig*)](III) is given on table 1.

The density of GXC is 1.5 g/cm^3, the density of the P(VP-*co*-MABA) copolymer is 1.4 g/cm^3, the density of ZrO_2 is approximately 6 g/cm^3. Thus, volume fractions of components in air-dry composite films (organic-inorganic hybrid material) varied as follows: from 99.98 to 59.8 wt.% for GXC, from 0 to 33.3 wt.% for ZrO_2 NPs, and from 0.02 to 2.5 wt.% for Tb^{3+}. The portion of MPC was 32-35 wt.% (table 1). The studied objects were rectangular films with the following dimensions: $l \times w \times h$ = 25 mm × 25 mm × (70÷150) μm.

2.3. Luminescence studies

Luminescence emission and excitation spectra of composites containing Tb^{3+} and other additives (table 1) were recorded using a LS-100 BASE luminescence spectrophotometer (PTI Lasers Inc., Canada) equipped with a solid sample holder. Luminescence intensity, I_{lum}, was registered in the direction of incident exciting light in the phosphorescence mode with a signal integration window of 100÷2000 μs. The glancing angle between exciting light beam and a sample was ~ 30°. The wavelength range of 460÷700 nm was used for emission spectra (the excitation wavelength λ_{ex} = 299 nm); the wavelength range of 210÷400 nm was used in observation of luminescence (the observation wavelength λ_{obs} = 543 nm). The used slit width of excitation and luminescence monochromators was 4 nm. Photomultiplier tube gain values were 200 and 500. For correct comparison, the measured values of I_{lum} were normalized by the internal laboratory standard.

Evaluation of luminescence efficiency of the composites, θ, was performed using the I_{lum} value of the luminescence band at λ_{max} = 543 nm; this maximum corresponds to the $^5D_4$ — $^7F_5$ transition of Tb^{3+} from the emission resonance level to the ground state, which demonstrates the maximum intensity.

2.4. Neutron measurements

The small-angle and ultra-small-angle neutron scattering measurements were performed on the KWS-2 and KWS-3 scattering facilities (FRM-II reactor, Garching, Germany). The KWS-2 facility is a classical SANS diffractometer operating in near point geometry. The measurements were performed at the neutron wavelength λ = 4.55 Å with $\Delta\lambda/\lambda$=0.1. The range of momentum transfer $3 \cdot 10^{-3} < q < 4.3 \cdot 10^{-1}$ Å^{-1} was obtained using three sample-to-detector distances S_D (2, 8 and 20 m). The scattered neutrons were detected by a two-dimensional position-sensitive detector (128×128 cells with a spatial resolution of 5 mm × 5 mm) based on ^{6}Li glass scintillators.

The KWS-3 is a high-resolution SANS diffractometer running on the focusing mirror principle; it allows performing scattering experiments with high momentum transfer resolution up to 10^{-4} Å^{-1} [24, 25]. The measurements were performed at the neutron wavelength λ = 12 Å with $\Delta\lambda/\lambda$=0.2. The range of momentum transfer $2.5 \cdot 10^{-4} < q < 1.4 \cdot 10^{-2}$ Å^{-1} was obtained using two sample-to-detector distances *S*D (1 and 10 m). The scattered neutrons were detected by a two-dimensional position-sensitive detector (diameter of the active zone was 8.7 cm, spatial resolution was 0.36 × 0.39 mm2) based on ^{6}Li glass scintillators.

In both cases, films of preliminarily disintegrated air-dry GXC and GXC-based organic-inorganic composites were clamped between two quartz glass plates. The raw data were corrected using the standard procedures [26] taking into account the scattering from the setup equipment and quartz glasses plates. The resulting 2D isotropic spectra were averaged azimuthally and obtained 2D spectra of SANS and USANS were merged. Their absolute values were determined by normalization to the incoherent scattering cross section of plexiglas with inclusion of the detector efficiency [26] and

thickness L_s for each sample. All the measurements were done at room temperature. The QtiKWS software [27] was used for data processing.

The intensity of SANS and USANS analysed in this work ($I_s(q)$) was determined as:

$$I_s(q) = I(q) - T \cdot I_0(q) \quad (1)$$

where $I(q)$ and $I0(q)$ are the q-distributions of scattered neutrons after sample and neutron beam without sample, respectively; T is the transmission coefficient of the neutrons passed through a sample:

$$T = \frac{I(0)}{I_0(0)} = \exp(-\Sigma_{tot} \cdot L) \quad (2)$$

where $\Sigma = \sigma_s + \sigma_a$ is the integral cross-section including nuclear scattering σ_s and absorption σ_a; L is the sample thickness.

The measured values of SANS and USANS intensity are related to the scattering law $S(q)$ by the following equation:

$$I_s(q) = I_0 \cdot L \cdot \int F(q - q_1) S(q) dq_1 \quad (3)$$

where $F(q)$ is the function of instrument resolution which was approximated by the Gaussian function [28].

Thus, the use of these two methods (SANS and USANS) allowed us to obtain the complete picture of scattering by the polymer matrix prepared from preliminarily disintegrated air-dry GXC and GXC-based organic-inorganic composites in the q range from $2.5 \cdot 10^{-4}$ to 0.43 Å^{-1}, which corresponded to the analysing structure of the studied objects in the range of characteristic dimensions from 10 Å to several micrometers.

2.5. Measurements of Small-angle X-ray scattering

The measurements of small-angle X-ray scattering (**SAXS**) were carried out at the BioSAXS facility situated on the line 12P of the synchrotron PETRA III (DESY, Hamburg) and running in the axial geometry. Using photons of wavelength $\lambda = 0.124$ nm and the distance L = 3 m for the sample detector allowed to measure the scattering intensity in the range of momentum transferred $7 \cdot 10^{-3} \leq q \leq 1$ Å^{-1}. The installation is implemented with the gas-filled detector Pilatus 2M (Dectris) with the active area size equal to 253.7 × 288.8 mm and the pixel size equal to 172 × 172 μm^2.

Source spectra were corrected with taking into account the scattering by accessories, adhesive tape, and the background of the hall. The two-dimensional isotropic spectra obtained were azimuthally averaged with due regard for the efficiency of the detector. All measurements were performed at ambient temperature. For pre-processing of data, one used the ATSAS software package [29].

It should be noted that use of small-angle X-ray scattering, which is complementary to SANS, gave us opportunity to obtain additional information about the structure of the polymer matrix prepared from preliminarily disintegrated air-dry GXC and GXC-based organic-inorganic composites in the range of typical sizes not exceeding *ca.* 500 Å.

2.6. Scanning electron microscopy

In parallel with SANS and X-ray scattering experiments, microstructure of films was studied with the use of a Carl Zeiss N Vision 40 scanning electron microscope. Films were not subjected to any special treatment (e.g., coating with metal). Microphotographs were taken at an accelerating voltage of 1 kV.

2.7. The low-temperature nitrogen adsorption

The determination of specific surface area S_{sp} for films of organic-inorganic composites based on the polymer matrix of the air-dry pre-disintegrated GXC was performed by low-temperature nitrogen adsorption using a commercial QUADRASORB SI instrumentation. Before measuring, the samples were degassed at 80° C under vacuum for 5 ÷ 7 hours, depending on a sample. Based on the data

obtained, one calculated specific surface area S_{BET} using the Brunauer–Emmett–Teller (BET) equation on six points.

3. Results and discussion

3.1. Luminescence studies

Luminescence of hybrid polymer-inorganic GXC-based nanocomposites is provided by the presence of Tb^{3+} in the form of $TbCl_3$ and [Tb(*polyLig*)](III). The content of Tb^{3+} in composites was varied in order to find the optimal luminescence behaviour which reflects interaction between ZrO_2 NPs and the matrix in composites (compare samples K1, K2 and K4 in table 1). So, one of our tasks was to determine whether NPs are aggregated in the matrix, i.e. whether the GXC matrix is capable of dispersing ZrO_2 over the whole volume at the expense of possible hydrogen bonds. Since terbium (III) ions are able to adsorb on both the surface of NPs and the crystalline nanofibrils of GXC, it was necessary to reveal whether possible aggregation of NPs affect luminescence properties of the films. Figure 1 presents luminescence spectra of the composites containing varied amount of Tb^{3+} in the form of salt or MPC (with and without ZrO_2 NPs).

Analysis of luminescence spectra demonstrates the presence of characteristic bands at 490, 543, 580 and 620 nm within the luminescence band; these peaks can be compared with resonance transitions in luminescence spectra of Tb^{3+} corresponding to spectral terms $^5D_4 - {}^7F_J$, where J = 6—0 [12, 23, 30].

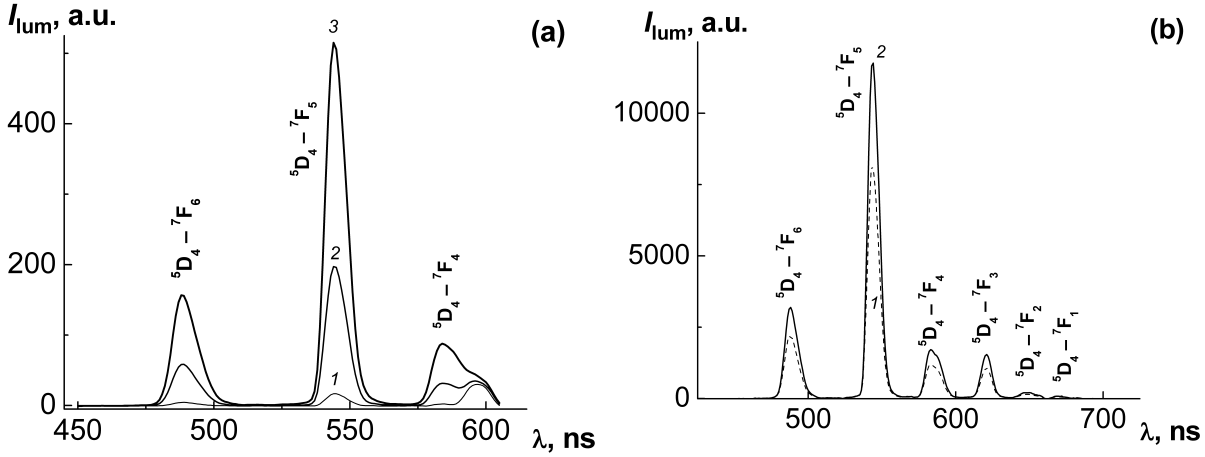

Figure 1. Luminescence spectra of Tb^{3+} in the form of $TbCl_3$ in the GXC matrix (a) for K1 (*1*), K2 (*2*), and K4 (*3*), or in the form of MPC in the composites based on GXC (b) for K7 (*1*) and K8 with added ZrO_2 NPs (6 wt.%) (*2*). The excitation wavelength was 300 nm. PMT gain was 500.

We have characterized luminescence efficiency of the studied composites with the value, θ, estimated from luminescence spectra using the following equation:

$$\theta = \frac{I_{300} / c_{Tb(III)}}{I_{300}^{K1} / c_{Tb(III)}^{K1}}, \quad (4)$$

where I_{300} is the luminescence intensity of a composite during excitation by light with a wavelength of 300 nm; $c_{Tb(III)}$ is the content of terbium (III) ions in a composite (wt.%); K1 is the superscript which indicates that the value applies to the composite K1 (table 1).

As seen from table 1, the efficiency value of θ varies little within the wide range of luminophore (*viz* Tb^{3+}) concentration from 0.02 to 1 wt.% (*note* K1 and K2 in table 1). However, increase in luminophore concentration up to 2.5 wt.% results in sharp decrease in the θ value from 1.43 to 0.33

(*note* K2 and K4 in table 1). At that, the total luminescence intensity I_{lum} increases (figure 1 (a)), though. These facts indicates the mode of concentration quenching has not set in, yet.

Assessment of luminescence efficiency through the value θ estimated demonstrated that the optimal content of Tb^{3+} is 0.21 wt.% (0.54 μmol per 40 mg of dry GXC); this value corresponds to terbium content in the composite K2. We have also obtained luminescence spectra of the composites containing [Tb(*polyLig*)](III) (figure 1 (b)). It was established that luminescence efficiency characterized by θ for the composites K7 and K8 are significantly higher than that in the case of low molecular weight luminophore $TbCl_3$ (compare with the values of θ for K1 and K2 on table 1). This result can be explained by antenna effect arising due to the formation of complex between Tb^{3+} and ligand fragment of monomer unit (*viz* 2-*o*-aminobenzoic acid) [23]. The suggested structure of [Tb(*polyLig*)](III) is shown in figure 2. The energy of exciting light (300 nm) is efficiently transferred to excited resonance nuclear level of terbium (III) ion according to the Förster resonance energy transfer mechanism (FRET) and then is transformed into visible radiation with large pseudo-Stokes shift [12].

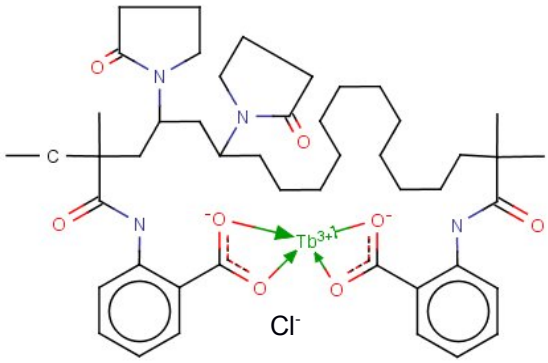

Figure 2. Scheme of [Tb(*polyLig*)](III) that includes P(VP-*co*-MABA) (88:12%).

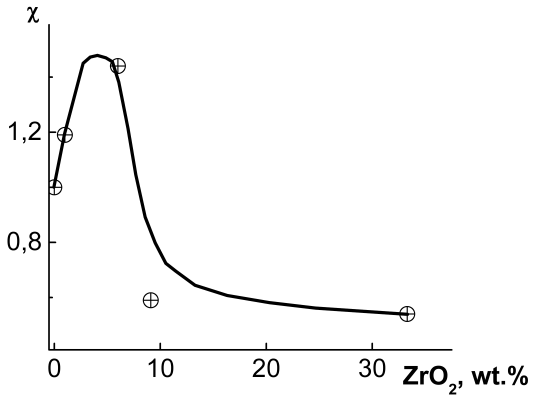

Figure 3. Enhanced luminescence of Tb^{3+} ions in GXC-based composites with adding ZrO_2 NPs. The observation wavelength is 543 nm.

Luminescence of Tb^{3+} in composites containing ZrO_2 NPs (*note* K3, K5, K6, and K8 in table 1) was also investigated. Analysis of luminescence spectra of these composites showed the presence of bands attributed to Tb^{3+} emission (*note* curve 2 in figure 1 (b)). Calculation of the values of θ characterizing luminescence efficiency in this case demonstrated increase in the value of I_{lum} in composites containing MPC with small amount of ZrO_2 NPs (not exceeding 6 wt.%).

The χ parameter characterizing enhancing luminescence upon addition of NPs was defined in compliance with:

$$\chi = \frac{\theta_{ZrO_2}}{\theta_{bm}}, \quad (5)$$

where θ_{ZrO_2}, θ_{bm} are the luminescence efficiency values of ZrO_2-containing composites and the corresponding composites without ZrO_2 as *benchmarks*, respectively. Variation of this parameter is shown in figure 3. It turned out that maximum luminescence is observed in the ZrO_2 concentration range of 1 to 6 wt.%. This fact may be related to change in the refractive index and dielectric constant of the filler which facilitates enhancing internal reflectance of light in a composite and more complete

energy transfer to Tb^{3+} [31]. Further increase in ZrO_2 concentration in the polymeric matrix leads to luminescence quenching caused by beginning the aggregation of NPs.

3.2. SANS and USANS

Figure 4 shows experimental dependences of neutron scattering cross-section $d\Sigma(q)/d\Omega$ on momentum transfer q on a double logarithmic scale obtained in the experiments with the polymer matrix prepared from air-dry preliminarily disintegrated GXC nano-gel film and GXC-based organic-inorganic composites containing Tb^{3+} in the form of $TbCl_3$ (figure 4 (a)) or of [Tb(*polyLig*)](III) (figure 4 (b)) and ZrO_2 NPs. The samples of organic-inorganic composites for small-angle neutron scattering were selected on the basis of the data of luminescence measurements (*note* K4, K5, K7 and K8 on table 1).

It can be seen from the data presented in figure 4 that scattering curves corresponding to the polymer matrix and composites containing Tb^{3+} in the form of $TbCl_3$ or [Tb(*polyLig*)](III) have qualitatively similar character. The common feature of scattering curves for these samples is the presence of two ranges; one is located in the area of high ($> q_c$) momentum transfers, and the other is located in the area of low ($< q_c$) momentum transfers q. The point of crossover from one scattering regime to another lies at $q_c \approx 6.5 \cdot 10^{-3}$ Å^{-1}. At the same time, behaviour of scattering cross-section function $d\Sigma(q)/d\Omega$ before and after the crossover point obeys power laws $q^{-\Delta}$ with different exponents $\Delta = n_1$ and n_2, respectively.

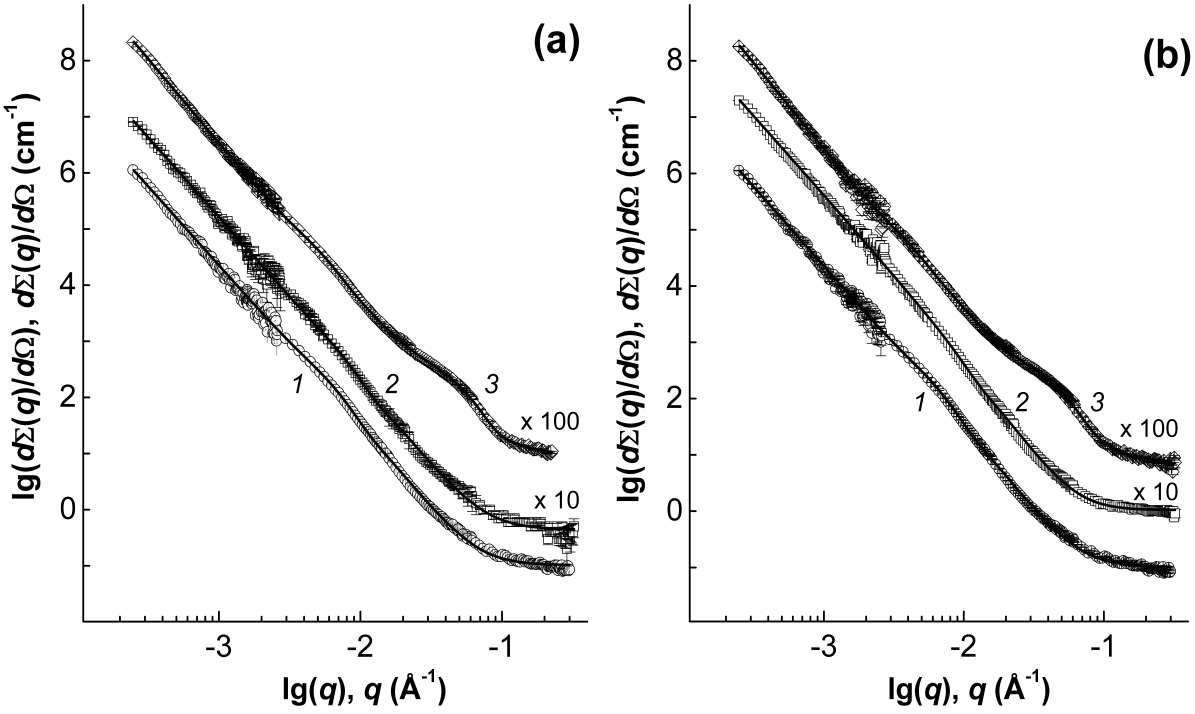

Figure 4. USANS and SANS differential cross sections $d\Sigma(q)/d\Omega$ in log-log scale for the matrix of GXC (*1*), and for the composites with Tb^{3+} in the form of $TbCl_3$ (a), and of MPC (b) without (*2*) and with ZrO2 NPs (*3*). Fits of experimental data by equation 7 are shown as solid lines. For the sake of clarity, cross section values for some samples were multiplied by 10 and 100 (corresponding factors are given next to the curves).

The scattering pattern observed for the studied films is typical of two-level hierarchical structures [30-33] with different characteristic scale and aggregation type for every level. The scattering from the first structural level (with lower scale) is observed in the area of high momentum transfers ($q > q_c$) and is described by the power dependence q^{-n_1}. The values of

exponent n_1 found from the slope of linear parts of experimental $d\Sigma(q)/d\Omega$ curves plotted on a double logarithmic scale are equal to 3.04 ÷ 3.05 ± 0.02; these values correspond to the scattering by inhomogeneities (clusters) possessing highly developed fractal surface [34]. Dimensionality of this surface can be defined as $D_{s1} = 6 - n_1 = (2.95 \div 2.96) \pm 0.02$. In this connection, in the subsequent analysis of scattering at $q > 6.5 \cdot 10^{-3}$ Å^{-1} we used the two-phase structure model (where pore is a solid phase) with fractal phase interface [35]. According to this model, the object consists of inhomogeneities (pores) with developed surface. Thus, if the total surface area of an inhomogeneity (pore) measured on a scale of its dimension R is proportional to R^2, measurement of its surface on a scale $r << R$ gives surface area of the order of $R^2(R/r)^{\Delta}$, where $0 < \Delta < 1$, and $n = 4 - \Delta$. Fractal dimensionality of surface ($D_s = 2 + \Delta$) is higher than 2.

Deviations of scattering cross-section curve $d\Sigma(q)/d\Omega$ from the q^{-n_1} power law are observed both in the vicinity of the crossover point q_c and in the area of high momentum transfers $q > 10^{-1}$ Å^{-1} for all samples. Near the crossover point q_c, this deviation is caused by the beginning of the Guinier regime [36], where scattering is determined by the characteristic size R_{c1} (in the case of fractal system, this is the upper boundary of self-similarity) independently of scattering fractal objects. Analysis of scattering in the Guinier regime (the slope of the $\ln(d\Sigma(q)/d\Omega)$ *vs.* q^2 plots) can give estimated radius of gyration R_{g1} of fractal objects and, correspondingly, their characteristic size R_{c1}. For example, in the case of spherical fractal objects, these values have the relation [37]:

$$R_{c1} = \left[(D_{s1} + 2)/D_{s1}\right]^{1/2} \cdot R_{g1}.$$

At $q > 10^{-1}$ Å^{-1}, scattering cross-section $d\Sigma(q)/d\Omega$ no longer depends on q (*i.e.*, becomes constant) and is apparently related to incoherent scattering by hydrogen atoms which are present in GXC in abundance. In this regard, analysis of the observed scattering and estimation of the lower boundary of self-similarity of fractal objects do not seem possible.

The scattering from the second (larger) structural level observed in the $q < q_c$ area is described by the q^{-n_2} power dependence. The values of exponent n_2 found from the slope of linear parts of experimental $d\Sigma(q)/d\Omega$ curves vary from 2.80 ± 0.07 (for the polymer matrix) to 2.87 ± 0.04 (for the composite containing Tb^{3+} in the form of MPC). It is known [34] that these values are typical of scattering from mass fractals (aggregates) with fractal dimensionality $2.80 \pm 0.07 \le D_{m2} = n_2 \le 2.87 \pm 0.04$.

The lower boundary of self-similarity of mass fractals on this structural level is determined by characteristic size R_{c1} of surface fractals (clusters) of the first structural level. In turn, absence of deviation of scattering curves at low q (figure 4) from power dependence (*i.e.*, transition to the Guinier regime) indicates that characteristic size of inhomogeneities R_{c2} exceeds the maximum size of inhomogeneities $R_{max} \approx 3.5/q_{min}$ [35]. The latter value is the maximum size of scattering objects which can be experimentally registered at a given resolution of an instrument. In our case, $q_{min} = 2.5 \cdot 10^{-4}$ Å^{-1} and, correspondingly, $R_{c2} > R_{max} \approx 14000$ Å.

As seen from figure 4, addition of ZrO_2 NPs together with Tb^{3+} (both in the form of low molecular weight salt $TbCl_3$ and MPC) leads to the appearance of an additional shoulder on the corresponding scattering curves (in the Guinier area) at $q > 1.8 \cdot 10^{-2}$ Å^{-1}. Here, scattering is determined by the characteristic size of independent scattering inhomogeneities R_{c0} and the related power dependence q^{-n_0}. Analysis of this dependence can give information about local structure of these inhomogeneities. The values of exponent n_0 found from the slope of linear parts of experimental $d\Sigma(q)/d\Omega$ curves are equal to 4.14 ± 0.06 and 4.30 ± 0.10 for the sample containing MPC and the sample without MPC, respectively. This scattering law is typical of porous systems with the so-called diffuse surface for which the exponent n is equal to $4 + 2\beta > 4$, where $0 \le \beta \le 1$ is the exponent characterizing the law of change in nuclear density ρ in the surface layer of inhomogeneities [38].

Let us suppose that inhomogeneities have virtually smooth surface, then nuclear density ρ would depend only on the distance x from a point on the surface. Therefore, nuclear density $\rho(x)$ can be presented as:

$$\rho(x)=\begin{cases} 0, & x<0 \\ \rho_0(x/\alpha)^{\beta}, & 0\le x\le\alpha \\ \rho_0, & x>\alpha \end{cases} \quad (6)$$

The parameter, α, is the width of the intermediate ("diffuse") layer where nuclear density ρ increases from zero to ρ_0. In this case, the appearance of the "diffuse" layer apparently results from modification of surface of ZrO_2 NPs with accompanying components (Tb^{3+} in the form of low molecular weight salt $TbCl_3$ or of MPC) which are used in the synthesis. From this assumption, in further analysis of scattering in the q area above $1.8\cdot10^{-2}$ Å^{-1} by the samples containing ZrO_2 NPs, the two-phase model (solid phase and pore) with diffuse phase interface [38] was used.

From the analysis of scattering in the Guinier regime (slope of dependences between $\ln(d\Sigma(q)/d\Omega)$ and q^2), we made the following estimates: R_{g0} = 87 ± 3 and 77 ± 8 Å and estimated characteristic dimensions ($R_{c0}=\sqrt{5/3}R_{g0}$ = 112.2 ± 3.9 Å) for the sample with and without MPC, respectively. The obtained estimated values indicate that "additional" scattering observed in the case of composites containing ZrO_2 NPs can be attributed to scattering by almost spherical ZrO_2 NPs with "diffuse" surface and diameter d_{c0} ~ 200 Å. Besides, correlation between the values of d_{c0} and dimensions of NPs (d_{ZrO2} = 200 ± 50 Å) used in the synthesis confirms the absence of aggregation of these particles. Difference in the values of d_{c0} and the β exponent for composites obtained without and with MPC is apparently related to different types of interaction between modifying additives and the surface of ZrO_2 NPs. In the first case, low molecular weight complexes containing Tb^{3+} are adsorbed on the surface of NPs as a thin layer, and in the second case, a thick layer of MPC (not less than 13 Å) covers the surface of ZrO_2 NPs.

It should be noted that in the region of low q (less than $1.8\cdot10^{-2}$ Å^{-1}), the shape of these scattering curves is similar to those observed for both the matrix of air-dry disintegrated GXC and its composites without ZrO_2, *i.e.*, these curves also include two regions with power dependence $d\Sigma(q)/d\Omega \sim q^{-\Delta}$ and different values of exponent ($\Delta = n_1$ and n_2). The first region is attributed to scattering by clusters with developed fractal surface and dimensionality D_{s1} = 2.85 ± 0.02 (independent of the presence of MPC in a composite). At the same time, use of MPC in the synthesis of hybrid organic-inorganic composites containing ZrO_2 NPs has a considerable effect on morphology of a higher structural level, which is described by power dependence q^{-n_2}, and this assumption is confirmed by estimation of values of the $n2$ exponent. Thus, for composite with ZrO2 NPs without MPC, n_2 = 2.96 ± 0.04, which corresponds to scattering by mass fractal aggregates with dimensionality D_{m2} = 2.96 ± 0.04 (similarly to the case of polymer matrix prepared from air-dry disintegrated GXC). On the other hand, introducing ZrO_2 NPs together with MPC into this GXC matrix leads to changes in the structure of the formed large scale aggregates. From the estimated value n_2 = 3.04 ± 0.03, we can conclude that surface fractals are formed instead of mass fractals. In other words, in this case, the second structural level of a composite is comprised of aggregates with highly developed fractal surface and dimensionality D_{s2} = 2.96 ± 0.02.

Thus, the SANS pattern observed for film of air-dry previously disintegrated GXC and GXC-based hybrid organic-inorganic composites containing Tb^{3+} in the form of low molecular weight salt or MPC as well as ZrO_2 NPs clearly indicates that these films contain two types of scattering inhomogeneities which differ strongly in their characteristic scale. Most likely, these samples consist of large-scale (R_{c2} > 14000 Å) mass fractal aggregates; in the case of composites containing ZrO_2 NPs together with MPC, these aggregates are constructed from surface fractal clusters with characteristic dimensions:

$$R_{c1}=\left[(D_{s1}+2)/D_{s1}\right]^{1/2}\cdot R_{g1}.$$

Addition of ZrO_2 NPs into composites leads to uniform distribution of these particles in the polymer matrix and absence of aggregation. Based on the above observations, in the detailed analysis of the scattering pattern observed for films of air-dry previously disintegrated GXC and GXC-based hybrid organic-inorganic composites containing Tb^{3+} in the form of low molecular weight salt or MPC as well

as ZrO_2 NPs, we used unified exponential/power law expression which takes into account the presence of several structural levels in the scattering system [39]:

$$\frac{d\Sigma(q)}{d\Omega} = \sum_{i=0}^{m} (G_i \cdot \exp\left(-\frac{q^2 R_{gi}^2}{3}\right) + B_i \exp\left(-\frac{q^2 R_{g(i-1)}^2}{3}\right)\left[\frac{(erf(qR_{gi}/\sqrt{6}))^3}{q}\right]^{n_i}) + I_{inc} \quad (7)$$

Summation in equation 7 is taken with respect to all structural levels. In the general case, equation 7 provides for the presence of 4 free parameters for every structural level, *i.e.* G_i (the Guinier prefactor), R_{gi} (radius of gyration), B_i (power-law prefactor) and n_i (the exponent). The parameter, I_{inc}, is a certain constant which does not depend on q and results from incoherent scattering by hydrogen atoms.

For obtaining final results, equation 7 was convoluted with the resolution function of the instrument. Experimental dependences of differential scattering cross-section $d\Sigma(q)/d\Omega$ were processed using the least squares method over the whole studied range. The results of this analysis are presented in figure 4 and in table 2.

Table 2. Structural parameters of the polymer matrix (air-dry pre-disintegrated GXC nano-gel film) and of hybrid organic-inorganic GXC-based composites, obtained from the SANS and USANS data.

System	R_{c0}, Å	$n_0 = 4 + 2\beta$	R_{c1}, Å	$n_1 = 6 - D_{s1}$	R_{c2}, Å	$n_2 = D_{m2}$; $6 - D_{s2}$
K0{Polymer matrix}	–	–	516 ± 26	3.05 ± 0.01		2.80 ± 0.07
K4{GXC / Tb^{3+}}	–	–	517 ± 25	3.04 ± 0.02		2.84 ± 0.04
K5{GXC / ZrO_2 / Tb^{3+}}	99.3 ± 10.3	4.30 ± 0.10	522 ± 19	3.15 ± 0.02	> 14000	2.96 ± 0.04
K7{GXC / Tb^{3+}+(MPC)}	–	–	548 ± 29	3.04 ± 0.02		2.87 ± 0.04
K8{GXC / ZrO_2 / Tb^{3+}(MPC)}	112.2 ± 9.5	4.14 ± 0.06	552 ± 20	3.15 ± 0.02		3.04 ± 0.03

3.3. SAXS

It is known [6] that GXC nano-gel film consists of water virtually to the extent of 90% and, correspondingly, the products based on this film contain rather high amounts of water. Thus, analysis of experimental SANS data for films of air-dry previously disintegrated GXC and GXC-based hybrid organic-inorganic composites in the area of $q > 0.15$ Å^{-1} was practically impossible due to the presence of strong background incoherent scattering by hydrogen atoms. At the same time, it is known [36] that amplitude of SAXS by an atom with atomic number Z (containing Z electrons) is directly proportional to Z. Thus, contribution of scattering by hydrogen atoms into small-angle scattering cross-section $d\Sigma(q)/d\Omega$ is negligible in comparison with contribution of atoms of other elements which are present in the studied samples (carbon, oxygen, terbium and zirconium). It was also necessary to increase the studied q range in order to obtain information about mesostructure on larger scale. In this connection, we carried out additional studies of the polymer matrix and cellulose-based hybrid organic-inorganic composites by SAXS. The corresponding SAXS curves are presented on a double logarithmic scale in figure 5.

It can be seen that behaviours of SAXS curves $I_S(q)$ measured for films of air-dry previously disintegrated GXC and composites containing Tb^{3+} in the form of $TbCl_3$ or of MPC are qualitatively similar. Scattering curves include two regions: high values of momentum transfer $q > q_c$ and low values of momentum transfer $q < q_c$, where q_c is equal to *ca.* $8.0 \cdot 10^{-1}$Å^{-1}. Behaviour of scattering intensity curve $I_S(q)$ obeys power laws $q^{-\Delta}$ with different values of exponent $\Delta = n_1$ and n_0, respectively. As was stated above, this pattern is typical of scattering by hierarchical two-level structures with different characteristic scale and type of aggregation for each level.

The scattering by the first of these structural levels (small-scale) is observed in the region of high momentum transfer ($q > q_c$) and described by power law dependence q^{-n_0}. The values of the n_0 exponent vary from 3.56 to 3.63, this corresponding to scattering by inhomogeneities (particles) with developed fractal surface and dimensionality $2.44 \le D_{s0} = 6 - n_0 = 2.37$. Deviations of the $I_S(q)$ scattering curve from the power law q^{-n_0} are observed in the vicinity of the crossover point $q_c \approx 8.0 \cdot 10^{-1}$ Å^{-1}; position of this point allows estimating characteristic dimension (upper limit of self-similarity) $R_{c0} = \left[(D_{s0}+2)/D_{s0}\right]^{1/2} \cdot R_{g0}$ of particles with fractal surface. Deviations are also observed for all samples in the region of high momentum transfers, where scattering intensity $I_S(q)$ does not depend on q and is related to incoherent scattering by inhomogeneities with scattering density ρ and dimensions of the order of wavelength of the used irradiation λ.

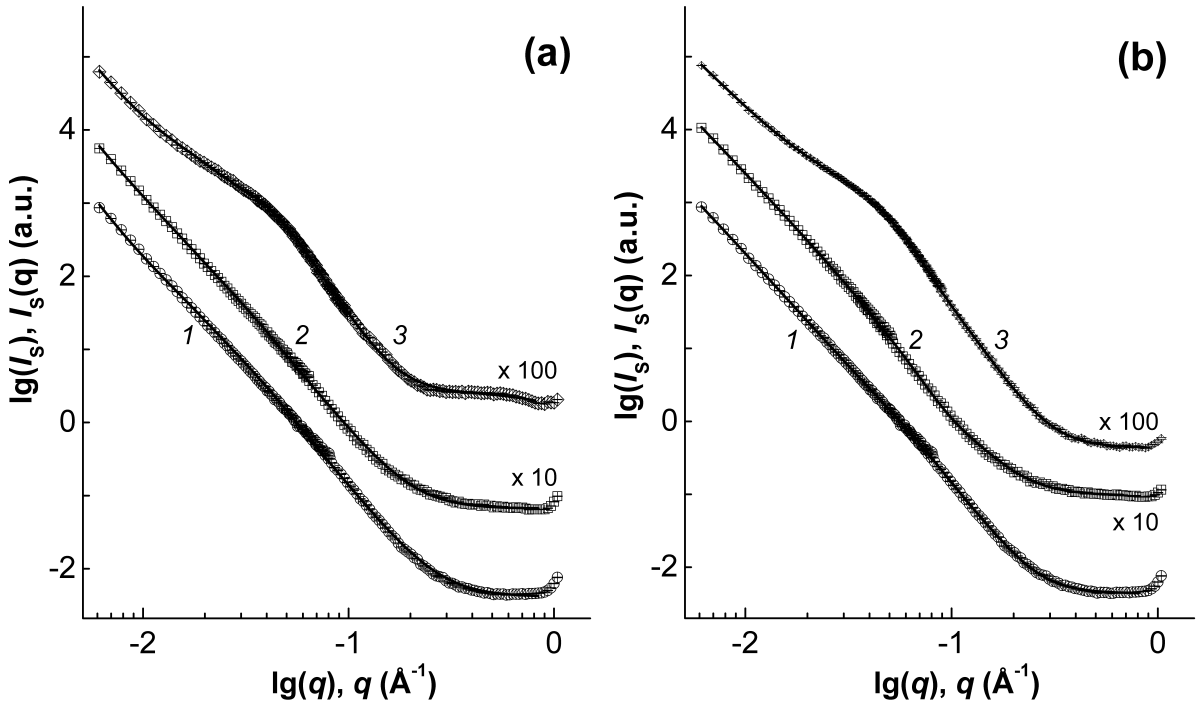

Figure 5. SAXS intensity in log-log scale for the matrix of GXC (*1*), and for composites with Tb^{3+} in the form of $TbCl_3$ (a), and of MPC (b) without (*2*) and with ZrO2 NPs (*3*). Fits of experimental data by equation 7 are shown as solid lines. For the sake of clarity, cross section values for some samples were multiplied by 10 and 100 (corresponding factors are given next to the curves).

Apparently, in the region of low q ($q < q_c$), SAXS observed for films of air-dry previously disintegrated GXC composites containing Tb^{3+} in the form of $TbCl_3$ or of MPC corresponds (similarly to SANS, *note* figure 4) to scattering by inhomogeneities (clusters) with highly developed fractal surface and dimensionality $2 \le D_{s1} = 6 - n_1 < 3$. This conclusion is confirmed by estimations of the $n1$ exponent obtained from the slopes of linear parts of experimental $I_S(q)$ curves; values of this exponent vary from 3.02 to 3.14. The lower limit of self-similarity of surface fractal clusters of this structural level is determined correspondingly by characteristic size R_{c0} of primary surface-fractal particles (inhomogeneities), and the upper limit of self-similarity R_{c1} was estimated earlier using SANS (table 2). The difference in values of fractal dimensionality D_{s1} obtained from the SANS and SAXS data is apparently related to difference in contrasts $\Delta\rho$ (solid phase-pore) of scattering densities for X-rays and neutrons.

The shape of SAXS curves $IS(q)$ obtained for hybrid organic-inorganic composites containing ZrO_2 NPs (figure 5) is similar to that of SANS curves in the region of momentum transfer values $q > 7 \cdot 10^{-3}$ Å^{-1}. Therefore, it can be concluded that the observed SAXS is also related mainly to scattering by almost spherical ZrO_2 NPs and nanoparticles with "diffuse" surface ($n_0 = 4 + 2\beta \approx 4.3$). It is virtually impossible to isolate contribution of the polymer matrix into scattering because of considerable difference between scattering density of GXC ($\rho_{GXC} = 1.34 \cdot 10^{11}$ cm^{-2}) and scattering density of ZrO_2 ($\rho_{ZrO_2} = 4.21 \cdot 10^{11}$ cm^{-2}). It should be noted that similar difference in the values of scattering density ρ is observed in SANS experiments; $\rho_{GXC} = 1.76 \cdot 10^{10}$ cm^{-2} and $\rho_{ZrO_2} = 5.04 \cdot 10^{10}$ cm^{-2}, respectively.

Thus, the use of SAXS allowed us to reveal another (primary) level in structural organization of the polymer matrix and GXC-based hybrid organic-inorganic composites.

In view of the above, in the detailed analysis of the small-angle X-ray scattering pattern observed for films of air-dry previously disintegrated GXC and GXC-based hybrid organic-inorganic composites, we also used the unified exponential/power law expression 7. For obtaining final results, equation 7 was convoluted with the resolution function of the instrument. Experimental dependences of SAXS intensity $I_S(q)$ were processed using the least squares method over the whole studied range. The results of this analysis are presented in figure 5 and in table 3.

Table 3. Structural parameters of the polymer matrix (air-dry, pre-disintegrated GXC nano-gel film) and of hybrid organic-inorganic GXC-based composites, obtained from the SAXS data.

System	R_{c0}, Å	$n_0 = 6 - D_{s0}$; $4 + 2\beta$	R_{c1}, Å	$n_1 = 6 - D_{s1}$
K0{Polymer matrix}	42.0 ± 3.2	3.63 ± 0.03		3.07 ± 0.01
K4{GXC / Tb^{3+}}	50.7 ± 4.1	3.56 ±0 .04		3.14 ± 0.01
K5{GXC / ZrO_2 / Tb^{3+}}	105.5 ± 5.6	4.32 ± 0.02	> 400	3.15 ± 0.01
K7{GXC / Tb^{3+}(MPC)}	104.5 ± 6.0	3.62 ± 0.02		3.02 ± 0.01
K8{GXC / ZrO_2 /Tb^{3+}(MPC)}	104.5 ± 5.5	4.29 ± 0.02		3.54 ± 0.03

The results obtained in the studies of the initial polymer matrix by complementary methods (USANS, SANS and SAXS, *note* tables 2 and 3) clearly indicate that this matrix is a porous system with three-level fractal structural organization. The lower structural level of the polymer matrix consists of almost spherical primary inhomogeneities with developed fractal surface, dimensionality $D_{s0} = 2.37 \pm 0.03$ and upper limit of self-similarity $R_{c0} = 42.0 \pm 3.2$ Å. These inhomogeneities form secondary surface fractal clusters with dimensionality $D_{s1} = 2.95 \pm 0.01$ and upper limit of self-similarity $R_{c1} = 516 \pm 26$ Å. It can be assumed that during biosynthesis of GXC nano-gel film, surface fractals of the second structural level aggregate to form large-scale ($R_{c2} > 1.4$ μm) mass fractals with dimensionality $D_{m2} = 2.80 \pm 0.07$.

Structural organization of hybrid organic-inorganic composites is similar to a large extent to that of the initial polymer matrix. All synthesized composites also demonstrate three-level fractal structure which is mainly formed by the initial polymer matrix. At the same time (tables 2 and 3) both composition and state of matter of the additives used in the synthesis exert considerable influence on morphology of the obtained composites.

Thus, introducing Tb^{3+} in the form of low molecular weight salt into the polymer matrix influences only structural parameters of the primary surface fractal inhomogeneities (*i.e.*, leads to increase in their fractal dimensionality D_{s0} from 2.37 to 2.44 and increase in their characteristic size R_{c0} from 42 to 50.7 Å). The structure of surface fractal clusters of the secondary structural level and large-scale mass fractal aggregates remains virtually unchanged. Therefore, it can be assumed that molecular

complexes containing Tb^{3+} are adsorbed on primary inhomogeneities, loosen their surface and lead to increase in their characteristic size R_{c0}.

At the same time, introducing Tb^{3+} in the form of MPC into the polymer matrix has virtually no influence on surface fractal dimensionality of the primary inhomogeneities D_{s0} and dimensionality of clusters D_{s1}, but leads to considerable increase in their characteristic sizes R_{c0} and R_{c1}. Thus, the size of the primary inhomogeneities R_{c0} increases almost by a factor of 2.5 (up to ≈ 105 Å), and the size of surface fractals of the secondary structural level increases from 516 to 548 Å, respectively. Apparently, MPC uniformly envelops both the primary inhomogeneities and surface fractal clusters and does not change their surface morphology. It should be noted that use of MPC as an additive also results in compacting of mass fractal aggregates (because voids between clusters are partially filled) and thus leads to increase in fractal dimensionality D_{m2} from 2.80 to 2.87.

Doping with ZrO_2 NPs together with Tb^{3+} (both in the form of low molecular weight salt and in the form of MPC) exerts the most pronounced influence on morphological structure of the initial polymer matrix. As it has been established previously, ZrO_2 NPs modified during synthesis are uniformly distributed in pores of surface fractal clusters and voids of large-scale mass fractals which are comparable in size to these particles. This process leads, first, to slight smoothing of cluster surface (i.e., decrease in their fractal dimensionality D_{s1} from 2.95 to 2.85), while their characteristic sizes R_{c1} remain practically unchanged within the uncertainty of measurements. Secondly, when low molecular weight salt is used as a second modifying additive, compacting of aggregates occurs (which displays itself in increase in their fractal dimensionality D_{m2} from 2.8 to 2.96). When ZrO_2 NPs are introduced into the polymer matrix together with MPC, type of fractals changes from mass fractals (D_{m2} = 2.95) to surface fractals (D_{s2} = 2.96). This structural transition is apparently related to complete filling voids between clusters which form spatial network of mass fractal aggregate by ZrO_2 NPs and MPC; thus, "dense" aggregate is formed. Surface of this aggregate consists of clusters with highly developed fractal surface.

Analysis of morphology of the first structural level of hybrid organic-inorganic composites containing ZrO_2 NPs is impossible due to significant difference between scattering density ρ_{ZrO_2} and scattering density of GXC (ρ_{GXC}). However, we can assume that mesostructure of the primary particles of bacterial cellulose NGF remains unchanged due to considerable difference in their sizes: $d_{c0}(ZrO_2)$ ~ 200 Å, and d_{c0}(GXC) ~ 80 Å.

The above-proposed model of the organization of the micro- and mesostructure of hybrid organic-inorganic composites based on polymer matrix of air-dry pre-disintegrated nano-gel GXC film is confirmed by the analysis of the experimental data obtained by low-temperature nitrogen adsorption and SEM. As can be seen from table 4, the obtained values of specific surface area, S_{BET}, clearly indicate that these composites have a porous structure with the sufficiently developed system of open pores.

Table 4. Specific surface area, S_{BET}, for hybrid organo-inorganic composites based on the polymeric matrix of air-dryed, pre-disintegrated nano-gel-film of GXC by low-temperature nitrogen adsorption

System	S_{BET}, m^2/g
K4{GXC / Tb^{3+}}	141.5
K5{GXC / ZrO_2 / Tb^{3+}}	69.6
K7{GXC / Tb^{3+}(MPC)}	112.8
K8{GXC / ZrO_2 / Tb^{3+}(MPC)}	329.3

The composite being the closest in structural parameters to a polymeric matrix of GXC is received by doping with Tb^{3+} in the form of $TbCl_3$ (tables 2 and 3), with the value of S_{BET} making 141.5 m^2/g for it. At the same time, the porosity of the composites under investigation explicitly depends on the

chemical nature of the additives in the process of their synthesis. Thus, the use of [Tb(*polyLig*)](III), or of ZrO_2 NPs together with Tb^{3+} in the form of $TbCl_3$ significantly reduces the specific surface area, S_{BET}, for composites to 112.8 and 69.6 m^2/g, respectively. In the first case, it is apparently related to the increase in the characteristic dimensions of the primary inhomogeneities, R_{c0}, and of fractal clusters of the 2nd structural level, R_{c1} (tables 2 and 3). In the second one it is due to filling of the pores of the cellulose matrix with ZrO_2 NPs. The highest value of S_{BET} equal to 329.3 m^2/g was observed for the composite containing ZrO_2 NPs together with [Tb(*polyLig*)](III) (table 4). Obviously, the growth of S_{BET} for this composite is associated with a different nature of the fractal structure organization for the large aggregates of the third structural level, comparing to the initial polymer matrix of GXC and other composites based on it: That is with changing the fractal type from mass to the surface one.

Analysis of SEM images presented in figure 6 demonstrated that morphology of the polymer matrix obtained from air-dry previously disintegrated GXC nano-gel film changes in various composites depending on chemical nature of components. It is well-known [40] that morphology of GXC nano-gel film can be presented as a polymer network, which remains virtually unchanged in composites and after previous disintegration of GXC with subsequent drying this dispersion in air. In our case, SEM images illustrate the process of filling this network with various additives. Composites with [Tb(*polyLig*)](III) demonstrate more compact surface structures. This phenomenon is caused by the presence of flexible polymer in MPC. These microphotographs clearly demonstrate the third structural level which was detected by USANS.

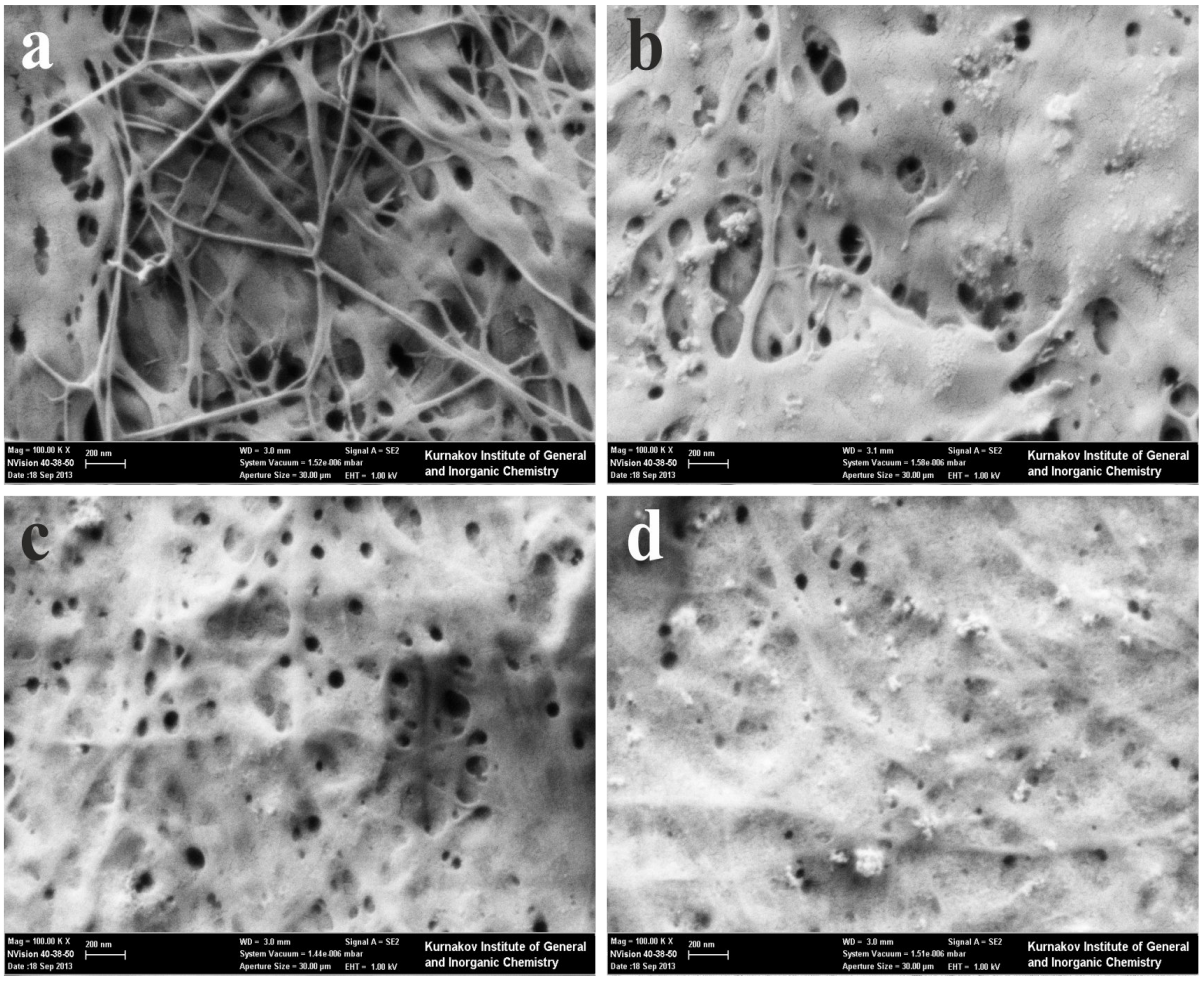

Figure 6. Microphotographs of GXC composites with Tb^{3+} in the form of $TbCl_3$ (a), and of MPC (b);

the analogous composites but with ZrO_2 NPs, respectfully (c, d). The scale bar is 200 nm.

4. Conclusions

Micro- and mesostructure, including fractal one, of the polymeric matrix prepared from air-dry, pre-disintegrated GXC, and of composites on its base with the addition of ZrO_2 NPs and Tb^{3+} in the form of $TbCl_3$ and in [Tb(*polyLig*)](III) was investigated by SEM techniques, USANS, SANS, and SAXS, as well as by low-temperature nitrogen adsorption.

Comprehensive analysis of the experimental data showed that the initial polymeric matrix is a porous system with a complex – three-level structure of the fractal organization. The lower structural level of the polymeric matrix consists of initial inhomogeneities being near-spherical and possessing a developed fractal surface with D_{s0} = 2.37 ± 0.03 and an upper limit of self-similarity R_{c0} = 42.0 ± 3.2 Å. Then these inhomogeneities formed the secondary surface fractal clusters with D_{s1} = 2.95 ± 0.01 and an upper limit of self-similarity R_{c1} = 516 ± 26 Å. On the third structural level, surface fractal clusters aggregate into large-scale (R_{c2} > 1.4 microns) mass-fractal aggregates with D_{m2} = 2.80 ± 0.07.

It is found that the structural organization of the hybrid organic-inorganic composites in many ways, and in the case of doping by Tb^{3+} almost entirely maintains the original character of the structural organization of the polymer matrix. For all of the synthesized composites, they are also characterized by a three-level fractal structure, in the formation of which the leading role is clearly belongs to the original polymer matrix.

At the same time, it was revealed that the composition and aggregation state of dopants used in the synthesis have a significant impact on the structural characteristics of the organic-inorganic composites. Thus, the introduction of Tb^{3+} in the form of $TbCl_3$, and as the part of [Tb(*polyLig*)](III) leads to increase of the characteristic size R_{c0} of initial inhomogeneities. Upon using MPC, the growth of the characteristic size R_{c1} of clusters of the *2nd* structural level was also observed, with their surface fractal dimension D_{s1} decreasing. In turn, it was found that the presence of doping ZrO_2 NPs in the composition has a significant impact only on the morphology of large-scale units of the *3rd* structural level as a consequence of the nanoparticle characteristic size R_{ZrO_2} equal to *ca.* 100 Å. This effect is resulting in the significant increase in the mass-fractal dimension D_{m2} of aggregates from 2.80 to 2.96 for the composite K5 {GXC / ZrO_2 / Tb^{3+}}, or in the change of a fractal type from the mass to the surface one for the composite K8 {GXC / ZrO_2 / [Tb(*polyLig*)](III)}. It clearly indicates more compact filling of the cellulose matrix by doping components.

Luminescence measurements have shown that upon using MPC with Tb^{3+} based on P(VP-*co*-MABA) as the luminophore, the efficiently luminescent composite materials were produced. Adding MPC in a polymer matrix allowed to overcome the concentration quenching in the matrix and made it possible to realize an efficient transfer of electronic excitation energy by the Förster mechanism from an *o*-aminobenzoic moieties to the central lanthanide atom due to the antenna effect. It is also found that the use of ZrO_2 NPs as doping ingredients at a concentration of from 1 to 6 wt.% can significantly enhance the luminescence of Tb^{3+} in the composite material due to a possible change in the refractive index of the composite.

Certainly, the results obtained can be used in the field of regenerative medicine, as well as in optoelectronics.

Acknowledgements

The work was financially supported by Program of Fundamental Research of Presidium of RAS # 1 “Nanostructures: physics, chemistry, biology, the basics of technologies” and Russian Foundation for Basic Research (grant № 16-02-00987A). We would like to express special thanks to Dr. Zhendong Fu (JCNS, Forschungszentrum Juelich GmbH, Outstation at MLZ, Garching, Germany) for support in performing the USANS experiments.

References

[1] Binnemans K 2009 Lanthanide-based luminescent hybrid materials *Chem. Rev.* **109** 4283–374

DOI 10.1021/cr8003983
Carlos L D, Ferreira R A S, Bermudez V de Z and Ribeiro S J L 2009 Lanthanide-containing light-emitting organic-inorganic hybrids: a bet on the future *Adv. Mater.* **21** 509–34 DOI 10.1002/adma.200801635

[2] Liao C, Zhang M, Yao M Yu, Hua T, Li L and Yan F 2015 Flexible organic electronics in biology: materials and devices *Adv. Mater.* **27** 7493–527 DOI 10.1002/adma.201402625
Nogi M and Yano H 2008 Transparent nanocomposites based on cellulose produced by bacteria offer potential innovation in the electronics device industry *Adv. Mater.* **20** 1849–52 DOI 10.1002/adma.200702559
Nogi M, Iwamoto S, Nakagaito A N and Yano H. 2009 Optically transparent nanofiber paper *Adv. Mater.* **21** 1595–98 DOI 10.1002/adma.200803174

[3] Czaja W K, Young D J, Kawecki M and Brown R M Jr 2007 The Future Prospects of Microbial Cellulose in Biomedical Applications *BioMacromolecules* **8** 1–12 DOI 10.1021/bm060620d

[4] Habibi You, Lucia L A and Rojas O J 2010 Cellulose Nanocrystals: Chemistry, Self-Assembly, and Applications *Chem. Rev.* **110** 3479–500 DOI 10.1021/cr900339w
Klemm D, Kramer F, Moritz S, Lindström T, Ankerfors M, Gray D and Dorris A 2011 Nanocelluloses: A New Family of Nature-Based Materials *Angew. Chem. Int. Ed.* **50** 5438–66 DOI 10.1002/anie.201001273
Eichhorn S J, *et al.* 2010 Review: current international research into cellulose nanofibres and nanocomposites *J Mater Sci* **45** 1–33 DOI 10.1007/s10853-009-3874-0
Chen P, Cho S Y and Jin H-J 2010 Modification and Applications of Bacterial Celluloses in Polymer Science *Macromolecular Research* **18** 309-20 DOI 10.1007/s13233-010-0404-5
Moon R J, Martini A, Nairn J, Simonsen J and Youngblood J 2011 Cellulose nanomaterials review: structure, properties and nanocomposites *Chem. Soc. Rev.* **40** 3941–3994 DOI: 10.1039/c0cs00108b

[5] Brown R M Jr, Saxena I M and Kudlicka 1996 Cellulose biosynthesis in higher plants *Trends in Plant Sciences* **1** 149–156 DOI:S1360-1385(96)10017-0
Baklagina Y G, Khripunov A K, Romanov D P, Klechkovskaya V V, Lavrent'ev V K, Smyslov R Y, Bugrov A N, Tkachenko A A, Romanov V N and Vinogradova K L 2012 Phase transitions of native celluloses from evolutionarily different sources into polymorph IV *Russian Journal of Applied Chemistry* **85** 1923-9 DOI 10.1134/S1070427212120018

[6] Brown R M Jr 1996 The biosynthesis of cellulose *J. M. S. – Pure Appl. Chem.* A **33** 1345–73
Huang Y, Zhu C, Yang J, Nie Y, Chen C and Sun D 2014 Recent advances in bacterial cellulose *Cellulose* **21** 1–30 DOI 10.1007/s10570-013-0088-z

[7] Klechkovskaya V V, Baklagina Yu G, Stepina N D, Khripunov A K, Buffat P A, Suvorova E I, Zanaveskina I S, Tkachenko A A and Gladchenko S V 2003 Structure of cellulose Acetobacter xylinum *Crystallography Reports* **48** 755–62

[8] Maria L C S, Santos A L C, Oliveira P C et al 2009 *Materials Letters* **63** 797-99
Baklagina Y G, *et al.* 2006 Interaction of Se^0 nanoparticles stabilized by poly(vinylpyrrolidone) with gel films of cellulose Acetobacter xylinum *Crystallography Reports* 51 619-26 DOI 10.1134/S1063774506040134
Khripunov A K, *et al.* 2007 Formation of a composite from Se^0 nanoparticles stabilized with polyvinylpyrrolidone and Acetobacter xylinum cellulose gel films *Russian Journal of Applied Chemistry* **80** 1549–57 DOI 10.1134/S1070427207090200
Volkov V V, Klechkovskaya V V, Shtykova E V, Dembo K A, Arkharova N A, Ivakin G I and Smyslov R Yu 2009 Determination of the Size and Phase Composition of Silver Nanoparticles in a Gel Film of Bacterial Cellulose by Small-Angle X-Ray Scattering, Electron Diffraction, and Electron Microscopy *Crystallography Reports* **54** 169–73 DOI 10.1134/S1063774509020011
Wang W, Zhang T J, Zhang D W et al 2011 *Talanta* **84** 71–7
Gutierrez J, Tercjak A, Algar I et al 2012 *Journal of Colloid and Interface Science* **377** 88–93

Yang Z, Chen S, Hu W et al. 2012 *Carbohydrate Polymers* **88** 173–78
[9] Buyanov A L, Gofman I V, Revelskaya L G, Khripunov A K and Tkachenko A A 2010 Anisotropic swelling and mechanical behavior of composite bacterial cellulose–poly(acrylamide or acrylamide–sodium acrylate) hydrogels *Journal of the mechanical behaviour of biomedical materials* **3** 102–11 DOI 10.1016/j.jmbbm.2009.06.001
[10] Buyanov A L, Gofman I V, Bozhkova S A, Saprykina N N, Kochish A Yu, Netyl'ko G I, Khripunov A K, Smyslov R Yu, Afanas'ev A V and Panarin E F 2016 *Russian Journal of Applied Chemistry* **89** 772-9 DOI 10.1134/S1070427216050141
Velichko E V, Buyanov A L, Chetverikov Yu O, Duif C P, Bouwman W G and Smyslov R Yu 2016 Mesostructure anisotropy of bacterial cellulose—polyacrylamide hydrogels as studied by spin-echo small-angle neutron scattering *Preprint* arXiv 1608.00544
[11] Lina F, Yue Z, Jin Zh and Guang Y 2011 Bacterial Cellulose for Skin Repair Materials *Biomedical Engineering – Frontiers and Challenges* ed R Fazel (Rijeka, Shanghai: InTech) chapter 3 pp 251-74 http://www.intechopen.com/books/biomedical-engineering-frontiers-and-challenges/bacterialcellulose-for-skin-repair-materials
[12] Bünzli J.-C. G. 2010 Lanthanide luminescence for biomedical analyses and imaging Chem. Rev. 110 2729–55 DOI 10.1021/cr900362e
[13] Werts M H V 2005 Making sense of lanthanide luminescence *Sci. Prog.* **88** 101–31
[14] Blasse G and Grabmaier B C 1994 *Luminescent Materials* (Berlin: Springer)
Justel T, Nikol H and Ronda C 1998 *Angew. Chem. Int. Ed.* **37** 3085
[15] Bugrov A N, Rodionov I A, Zvereva I A, Smyslov R Y and Almjasheva O V 2016 Photocatalytic activity and luminescent properties of Y, Eu, Tb, Sm and Er-doped ZrO_2 nanoparticles obtained by hydrothermal method International *Journal of Nanotechnology* **13** 147–57
[16] Marling J, 1978 1.05-1.44 micron tunability and performance of the CW Nd/3+/:YAG laser *IEEE J. Quantum Electron.* **14**, 56–62 DOI 10.1109/JQE.1978.1069667
[17] Kuriki K, Koike Y, Okamoto Y, 2002 *Chem. Rev.* **102** 2347
[18] Polman A, van Veggel F C J M, 2004 *J. Opt. Soc. Am.* B **21** 871
[19] Legnani C. *et al.* 2008 *Thin Solid Films* **517** 1016–1020
[20] Patent RU №2141530
Patent RU №2189394
[21] Baklagina Yu G, *et al.* 2003 *Russian Journal of Applied Chemistry* **76** 989-96
[22] Bugrov A N and Almjasheva O V 2013 Effect of hydrothermal synthesis conditions on the morphology of ZrO_2 nanoparticles. *Nanosystems: Physics, Chemistry, Mathematics* **4** 1–6
[23] Yakimanskii A V, Goikhman M Y, Podeshvo I V, Anan'eva T D, Nekrasova T N and Smyslov R Y 2012 Luminescence of Ln^{3+} Lanthanide Complexes in Polymer Matrices *Polymer Science* A **54** 921-41 DOI 10.1134/S0965545X1209009X
[24] Radulescu A, *et al.* 2005 *Neutron News* 2005 **16** 7
[25] Goerigk G and Varga Z. 2011 *J. Appl. Cryst.* **44** 337
[26] Wignall G D and Bates F S 1987 *J. Appl. Cryst*. **20** 28
[27] http://iffwww.iff.kfa-juelich.de/~pipich/dokuwiki/doku.php/qtikws
[28] Schmatz W, Springer T, Schelten J and Ibel K. 1974 *J. Appl. Cryst* **7** 96
[29] https://www.embl-hamburg.de/biosaxs/download.html
Petoukhov M V, Franke D, Shkumatov A V, Tria G, Kikhney A G, Gajda M, Gorba C, Mertens H D T, Konarev P V and Svergun D I 2012 New developments in the ATSAS program package for small-angle scattering data analysis *J. Appl. Cryst.* **45** 342–50 DOI 10.1107/S0021889812007662
[30] Carnall W T 1979 *Handbook on the Physics and Chemistry of Rare Earths* vol 3, ed K A Gschneidner Jr and L Eyring (Amsterdam: North Holland Publ. Co.) p 172
[31] Reisfeld R, Zelner M and Patra A 2000 Fluorescence study of zirconia films doped by Eu, Tb and Sm and their comparison with silica films *Journal of Alloys and Compounds* **300–1** 147–

51
Fox M 2010 *Optical Properties of Solids (Oxford Master Series in Physics) 2nd ed* (Oxford: Oxford University Press)
[32] Beaucage G, Ulibarri T A, Black E P and Schaefer D W 1995 *Hybrid Organic-Inorganic Composites (ACS Symposium Series)* ed J Mark *et al.* (Washington, DC: American Chemical Society) p 97
[33] Štěpánek M, Matějíček P, Procházka K, Filippov S K, Angelov B, Šlouf M, Mountrichas G and Pispas S 2011 *Langmuir* **27** 5275–81
Gubanova N N, Kopitsa G P, Ezdakova K V, Baranchikov A E, Angelov B, Feoktystov A, Pipich V, Ryukhtin V and Ivanov V K 2014 Structure of zirconium dioxide based porous glasses *Journal of Surface Investigation. X-ray, Synchrotron and Neutron Techniques* **8** 963–71 DOI 10.1134/S1027451014050309
Khamova T V, Shilova O A, Kopitsa G P, Angelov B and Zhigunov A 2016 Effect of Biocidal Additives on the Mesostructure of Epoxy–Siloxane Bioactive Coatings *Journal of Surface Investigation. X-ray, Synchrotron and Neutron Techniques* **10** 113–22 DOI 10.1134/S1027451015060312
[34] Teixera J 1986 *On Growth and Form-Fractal and Non-Fractal Pattern in Physics* ed H E Stanley, N Ostrovsky (Boston: Martinus Nijloff)
[35] Bale H D and Schmidt P W 1984 *Phys. Rev. Lett.* **38** 596
[36] Guinier A 1939 *Ann. Phys.* **12** 161
[37] Guinier A, Frournet G, Walker C B and Yudowitch K L 1955 *Small-Angle Scattering of X-rays* (New York: Wiley) p 17
[38] Schmidt P W, Avnir D and Levy D *et al.* 1991 *J. Chem. Phys.* **94** 1474
[39] Beaucage G and Schaefer D W 1994 *J. Non-Cryst. Solids* **172–74** 797
[40] Svensson A, Nicklasson E, Harrah T, Panilaitis B, Kaplan D L, Brittberg M and Gatenholm P 2005 *Biomaterials* **26** 419–31